Bioactive Materials 19 (2023) 429–443

Contents lists available at ScienceDirect

Bioactive Materials

journal homepage: www.keaipublishing.com/en/journals/bioactive-materials

Reversing the imbalance in bone homeostasis via sustained release of SIRT-1 agonist to promote bone healing under osteoporotic condition

Wei Zhang [a,b,1], Xingzhi Zhou [a,b,1], Weiduo Hou [a,b,1], Erman Chen [a,b], Chenyi Ye [a,b], Mo Chen [c], Qian Lu [b,d,***], Xiaohua Yu [a,b,*], Weixu Li [a,b,**]

[a] Department of Orthopedics, Second Affiliated Hospital, School of Medicine, Zhejiang University, 310009, Hangzhou, China
[b] Research Institute of Orthopaedics, Zhejiang University, 310009, Hangzhou, China
[c] Department of Rheumatology, Second Affiliated Hospital, School of Medicine, Zhejiang University, 310009, Hangzhou, China
[d] Department of Orthopedics, Huzhou Hospital, Zhejiang University, China

ARTICLE INFO

Keywords:
Osteoporosis
Osteoblast
Osteoclast
Mineral coating
SIRT1

ABSTRACT

The imbalance of bone homeostasis is the root cause of osteoporosis. However current therapeutic approaches mainly focus on either anabolic or catabolic pathways, which often fail to turn the imbalanced bone metabolism around. Herein we reported that a SIRT-1 agonist mediated molecular therapeutic strategy to reverse the imbalance in bone homeostasis by simultaneously regulating osteogenesis and osteoclastogenesis via locally sustained release of SRT2104 from mineral coated acellular matrix microparticles. Immobilization of SRT2104 on mineral coating (MAM/SRT) harnessing their electrostatic interactions resulted in sustained release of SIRT-1 agonist for over 30 days. MAM/SRT not only enhanced osteogenic differentiation and mineralization, but also attenuated the formation and function of excessive osteoclasts via integrating multiple vital upstream signals (β-catenin, FoxOs, Runx2, NFATc1, etc.) *in vitro*. Osteoporosis animal model also validated that it accelerated osteoporotic bone healing and improved osseointegration of the surrounding bone. Overall, our work proposes a promising strategy to treat osteoporotic bone defects by reversing the imbalance in bone homeostasis using designated small molecule drug delivery systems.

1. Introduction

Osteoporosis, characterized by low skeletal mass, has been becoming a major healthcare concern in aging society. 8.9 million osteoporotic fractures occur worldwide each year [1]. About 1/2 of women experience an osteoporotic fracture in their lifetime as their bone mineral density dramatically drops after they enter menopause [2]. In clinic setting, the most common method for osteoporosis treatment remains systemic administration of drugs, including bisphosphonates, denosumab, parathyroid hormone (PTH), *etc*. Most of these drug function via an antiresorptive mechanism by inhibiting bone resorption during treatment. Moreover, these antiresorptive drugs also suffer from a slow onset of efficacy, which usually start to take effects in more than half a year. Such drawbacks of these drugs can often fail to provide structural support for implant fixation during the osteoporotic fracture treatment [3]. Thus, it is of great significance to increase the local bone density which enhance the holding force of internal implants in osteoporotic fractures management. In response to these challenges, local

Abbreviations: BMSCs, Bone marrow-derived mesenchymal stem cells; siRNA, Small interfering RNA; CCK-8, Cell Counting Kit-8; IF, Immunofluorescence; RT-qPCR, Quantitative real-time polymerase chain reaction; WB, Western blot; micro-CT, Microcomputed tomography; OVX, Ovariectomy; BMM, Bone marrow-derived macrophage; ALP, Alkaline phosphatase; OPN, Osteopontin; P1NP, Pro-collagen type 1N-terminal peptide; FBS, Fetal bovine serum; SBF, Simulated body fluid; SEM, Scanning electron microscopy; XRD, X-ray diffraction; FTIR, Fourier transform infrared.

Peer review under responsibility of KeAi Communications Co., Ltd.

* Corresponding author. Department of Orthopedics, Second Affiliated Hospital, School of Medicine, Zhejiang University, 310009, Hangzhou, China.
** Corresponding author. Department of Orthopedics, Second Affiliated Hospital, School of Medicine, Zhejiang University, 310009, Hangzhou, China.
*** Corresponding author. Research institute of Orthopaedics, Zhejiang University, 310009, Hangzhou, China.
E-mail addresses: zhangweilook@zju.edu.cn (W. Zhang), xingzhizhou@zju.edu.cn (X. Zhou), houweiduo@zju.edu.cn (W. Hou), chenerman@zju.edu.cn (E. Chen), yechenyi@zju.edu.cn (C. Ye), chenmo9105@zju.edu.cn (M. Chen), 121047919@qq.com (Q. Lu), Xiaohua.yu@zju.edu.cn (X. Yu), zrlwx@zju.edu.cn (W. Li).
[1] These authors contributed equally to this work.

https://doi.org/10.1016/j.bioactmat.2022.04.017
Received 14 January 2022; Received in revised form 14 April 2022; Accepted 15 April 2022

treatment strategies are proposed to prevent osteoporotic fracture, accelerate bone healing, and promote implant fixation by either enhancing anabolic pathways or inhibiting catabolic pathways. However, take into account that bone hemostasis is extremely complex, other physiological processes that are directly or indirectly related to bone should also be considered in the context of developing more effective localized osteoporosis treatments.

Although various drugs including proteins, polypeptides, antibodies, and small molecules have been used to increase bone density under osteoporotic condition, the clinical outcomes of osteoporosis management remain unsatisfactory. For instance, intermittent PTH administration induces bone formation, but the inconvenience of its repeated administration has limited its broader applications in clinic [4,5]. More recently, a series of novel molecules have been identified to simultaneously regulate multiple signaling pathways to achieve bone density/mass increase. Sirtuin 1 (SIRT1), a nicotinamide adenine dinucleotide-dependent deacetylase member exemplifies such potential molecule by showing capability to regulate multiple bone metabolism pathways. As reported by large body of literatures, SIRT1 can effectively upregulated Wnt/β-catenin and BMP-2 signaling pathways, which are both pivotal to the osteogenic differentiation of mesenchymal stem cells and osteoprogenitors [6–9]. Previous study demonstrated that SIRT1 supplement can decrease bone and muscle mass loss, slow aging, suppress the inflammatory response and delay multiple age-related diseases [10]. SIRT1 also attenuated osteoclastogenesis and suppressed bone resorption [6,11]. As such, SRT2104, a novel, first-in-class, highly selective small molecule activator of SIRT1 has successfully advanced through multiple phase I trials with few side effects to phase II trials due to its excellent tolerability and low systemic toxicity [9]. Compared to traditional SIRT1 activator resveratrol, the pharmacological potency of SRT2104 is more than 1000-fold greater [9,12], which make it an excellent candidate for osteoporotic bone healing. However, SRT2104 is currently administrated via oral route, which severely sacrifices its bioavailability and substantially increases dosage needed. Thus, local delivery of this molecule is worth exploring in order to further improve its therapeutic performance.

Drug delivery systems have been widely used in bone healing and other related diseases in the past three decades. Although bolus delivery of drugs via direct injection is commonly used in various fields, its therapeutic effect is severely limited by its short pharmaceutical kinetics. In contrast, sustained delivery strategies successfully bypassed the limitation of bolus delivery by providing local effective drug concentration for extended timeframe. A variety of formulations including scaffolds, microspheres, nanoparticles, and hydrogels, have been developed to accommodate the needs for sustained release systems. Currently, most of these delivery systems were designated for biomacromolecules such as growth factors, antibodies, genes, etc. as these macromolecules tend to diffuse slowly out of the carrier materials. However, most of these sustained systems are not suitable for small molecules drugs as they can quickly diffuse out of the carrier depot due to their small size and the large vacancy left after the formation of polymeric networks. In order to augment the therapeutic efficacy of small molecules drugs and harness them for sustained release delivery approaches for bone healing, there remains an urgent need for sophisticated delivery systems capable of precisely controlling small molecule release kinetics.

Our previous studies have shown the versatile molecule loading capacity of mineral coating formed by a biomimetic coating approach on biomaterials surface and implemented in various drug delivery systems [13,14]. Acellular tissue matrix has been used for tissue regeneration due to its similarity to natural ECM, bioactive components preservation, as well as its cell-responsive degradability. Plus, collagen, the major components of ECM, can effectively facilitate mineral coating growth on its surface [15]. Herein, harnessing the extraordinary drug release controllability, SRT2104 was immobilized on mineral coating formed on acellular matrix microparticles to form an injectable SRT2104 delivery system for in situ adjusting osteogenesis/osteoclastogenesis balance and promoting osteoporotic bone defects healing. In our study, we chose an acellular tissue matrix microparticles (AM) as base carrier material and formed a layer of mineral coating using modified simulated body fluid (mSBF) to serve as SRT2104 reservoir. SRT2104 was firmly immobilized onto the mineral coating via an electrostatic interaction between its molecular structure and the charged surface of mineral coating. The mineral coating interacts with the surrounding environment and degrades concurrently with the drug release. Our results demonstrated that the modified AM (MAM/SRT) displayed excellent biocompatibility and appropriate degradability and it also sustainably release SIRT2104 more than 30 days *in vitro*. As an upgraded highly-effective small molecule agonist for SIRT1, the sustained-release of SRT2104 provided a vital upstream signal to regulate multiple signaling pathways, thereby remarkably enhancing osteogenic differentiation and mineralization and inhibiting excessive osteoclastogenesis *in vitro*. Moreover, MAM/SRT accelerated the femoral bone healing of osteoporotic defect and promoted osseointegration of the surrounding bone *in vivo* (Fig. 1). Collectively, this study provides a promising and viable strategy for osteoporotic bone healing, which might hold value in its clinical transformation.

2. Results

2.1. Characterization of the MAM scaffolds

Porcine dermis derived acellular matrix microparticle was chosen as the base material for our delivery system due to its abundance in collagen, excellent biocompatibility, and appropriate degradability. We adopted a well-established decellularization protocol from our previous study to remove the cellular components from the dermis tissue [15]. As shown in Fig. 2-A, the residue DNA content dropped from 120 to 8 ng/mg, indicating that the decellularization treatment was highly effective. This treatment also decreased the fat content in the acellular matrix microparticles (AM) to 2% while slightly increased the collagen content after decellularization. HE staining clearly showed that no cellular components or cell nucleuses were visible after the treatment. This acellular matrix microparticles (AM) was then immersed in mSBF to form a layer of mineral coating on their surface. After 7 days of incubation in mSBF, coated AMs had a nanoporous, plate-like carbonate-substituted hydroxyapatite (cHAP) structure, which suggested the successful formation of mineral coated AM (MAM) (Fig. 2E). The pore size decreased due to the nanoporous mineral coating. The average pore size of AM is around 10 μm, whereas the average pore size of MAM becomes about 100 nm (Supplemental Fig. 1). Energy dispersive X-ray spectroscopy (EDS) showed that the presence of calcium and phosphorus elements in the mineralized coating and a calcium/phosphorus ratio 1.77, indicating that a certain extent of carbonate substitution took place during the formation of the coating, which might also be related to its degradability (Fig. 2F). Fourier transform infrared spectroscopy (FT-IR) and X-ray diffraction (XRD) also displayed characteristic peaks associated with carbonate and phosphate (Fig. 2G and H).

2.2. Binding and sustained release of SRT2104

SRT2104 was immobilized onto mineral coating surface of MAM via electrostatic interaction as shown in Fig. 3A. The amount of SRT2104 loaded on MAM can be easily controlled by changing the concentration of SRT2104 loading solution. The amount of SRT2104 bound on MAM increased linearly as the concentration of SRT2104 increased from 25 to 200 μg/mL (Fig. 3B). The drug loading efficiency and corresponding drug loading content in MAM/SRT were kept around ~95% except for 200 μg/mL group (Fig. 3B and C). Next, we found that SRT2104 binding to MAM was released in a sustained manner, and the release kinetics were dependent on the dissolution characteristics of the mineral coating [13]. The dissolution rate of the mineral coatings quantified by an

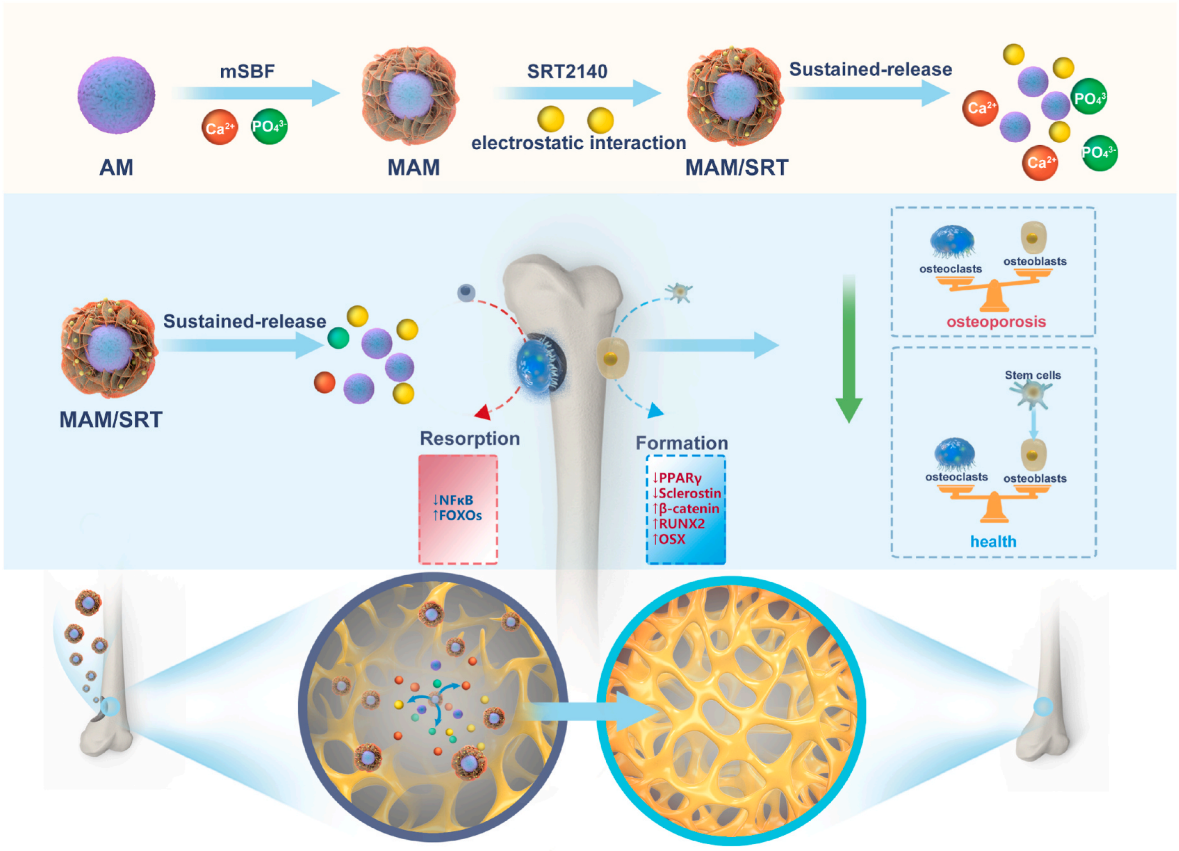

Fig. 1. A mineral coated acellular matrix microparticles to reverse the imbalance in bone homeostasis by simultaneously regulating osteogenesis and osteoclastogenesis vis locally sustained release of SRT2104. Red circles represent calcium ions. Green circles represent phosphorus ions. Yellow circles represent SRT2104.

Arsenazo III based assay showed that calcium was gradually released from MAM over 60 days regardless of SRT2104 loading amount (Fig. 3D). The phosphate amount released was measured by an acetone-acid-molybdate (AAM) based assay [16]. The results also showed that phosphate was gradually released from MAM over 60 days regardless of SRT2104 loading amount (Fig. 3E). As calcium and phosphate supply is a prerequisite for bone formation, thus release of calcium from MAM might be beneficial for osteoporotic bone defect healing [17]. Given the excellent efficiency and a sustained release kinetics, the concentration 10 mg/100 μg of MAM/SRT was selected for subsequent experiments *in vitro* and *in vivo*.

Meanwhile, degradation of acellular matrix microparticles was assessed by determining the free amine group in the release medium as ECM tends to degrade into amino acids. As shown in Fig. 3F, the concentration of free amino groups increased in the release medium during 2 weeks, suggesting that AM coated with mineral also started to degrade *in vitro*.

As shown in Fig. 3G, the release patterns of SRT2104 at various dosages displayed near-zero order release kinetics. Moreover, in the higher dosage groups, the release of SRT2104 was sustained for over 30 days, which solidly validated that MAM might server as a sustained release system for small molecules. The degradation of MAM/SRT (10 mg/100 μg/mL) was assessed at 2 weeks and 4 weeks in Fig. 3H. There was a significant absorption and degradation of mineralized coating on the surface of MAM/SRT.

This is pivotal for improving the efficacy of SRT2104 and alleviating the burden of administration for patients. SRT2104 needs to be taken daily when given orally, which not only diminish its pharmacological efficacy, but also increase the risk of potential systemic toxicity. A local sustained release system for SRT2104 can largely mitigates these drawbacks as when local effective concentration of the drug can be easily maintained using such system. Moreover, it also might substantially lower the overall dosage, which would both lower the cost and side effects once approved for clinical applications.

2.3. MAM/SRT did not affect cell proliferation and viability

Live/Dead staining, Cell Counting Kit 8 (CCK8) assay, and EdU fluorescence staining were used to assess the effects of MAM and MAM/SRT on cell proliferation and viability on days 1, 4, and 7.

As shown in Fig. 4A, dead cells were rarely detected and viable BMSCs proliferated rapidly in all three groups (Ctrl, MAM (1 mg), MAM/SRT (1 mg). Similar results were also obtained using CCK8 assay, suggesting that the presence of MAM have no impact on BMSCs proliferation (Fig. 4D).

Click-iT EdU assay was also performed to label cells progressing through S phase. No differences in mouse bone marrow-derived macrophages (BMMs) among these three groups were no detected (Fig. 4B and C). Overall, these results demonstrated that the mineral coated acellular matrix microparticles loaded with SRT2104 possess excellent biocompatibility and may be suitable as an implantable bone regeneration material.

3. MAM/SRT promoted osteogenic differentiation of BMSCs

Bone marrow mesenchymal stem cells (BMSCs) with multiple differentiation potential play an essential role in bone formation and bone hemostasis maintenance. To identify the effects of MAM/SRT on osteogenic differentiation of BMSCs, cells were treated with 0.1% DMSO (sham), 5 μM SRT2104 (SRT) [6,10], 0.1% DMSO + MAM (1 mg), or 0.1% DMSO + MAM/SRT (1 mg (10 mg/100 μg/mL)). Transwell inserts were placed in a 24-well plate to separate from the cells. Transwell

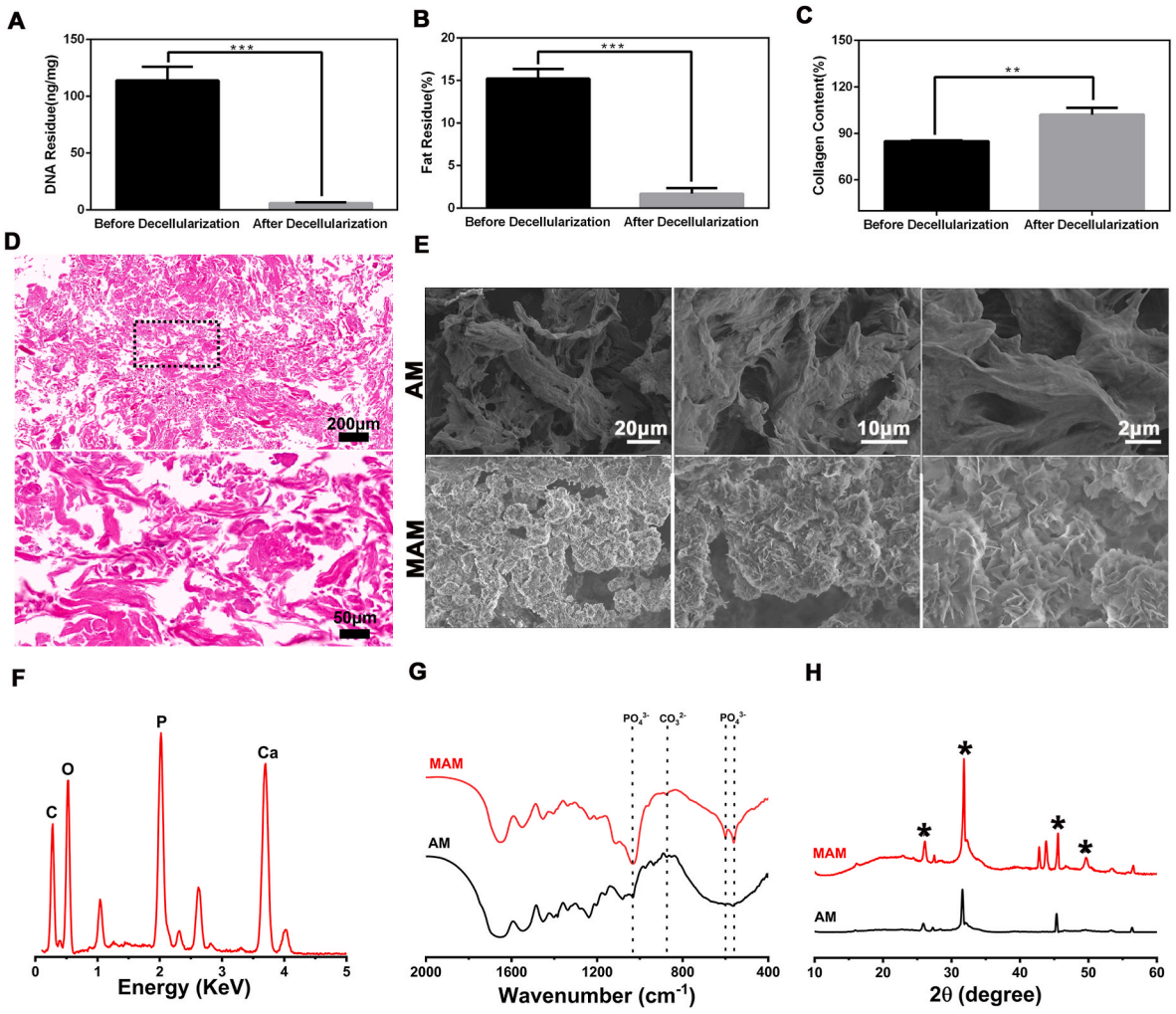

Fig. 2. A, Residue DNA content before and after decellularization. Data are expressed as the mean ± SD of three independent experiments, and one of three independent experiments is shown. *$p < 0.05$ vs. Before decellularization group. B, Residue fat content before and after decellularization. *$p < 0.05$ vs. Before decellularization group. C, Residue collagen content before and after decellularization. *$p < 0.05$ vs. Before decellularization group. D, HE staining of the base material after decellularization. E, SEM images of AM and MAM. F, Energy dispersive spectroscopy (EDS) of MAM. G, Fourier transform infrared spectroscopy (FT-IR) of AM and MAM. H, X-ray diffraction (XRD) of AM and MAM.

inserts were placed in a 24-well plate to separate from the cells. MAM and MAM/SRT were added into the upper chamber. The upper chamber was taken out using a tweezers with care and the medium in the lower chamber was then changed. Extreme care was taken to avoid materials loss during each manipulation. BMSCs in SRT group were treated with 5 μM SRT2104 every 3 days when the culture medium was changed. The other three group were treated with 0.1% DMSO every 3 days. During the process of osteogenic differentiation, BMSCs first differentiate toward osteoblast progenitor cells and then into mature osteoblasts that is characterized by some specific genes or proteins, including alkaline phosphatase (ALP), osteopontin (OPN), collagen type I (COL1), Runx2, bone sialoprotein, and osteocalcin. Runx2 has been identified as a master transcription factor to drive BMSCs into osteoblastic lineage [18]. Thus, the osteoblast-specific genes, including *Alp, Runx2,* and *Col1a1*, were evaluated by RT-qPCR on days 3 and 5 after osteogenic differentiation. As shown in Fig. 5A–F, compared with sham group, the SRT or MAM treatment resulted in only a minor increase in the mRNA levels of osteoblast-specific genes; whereas the MAM/SRT upregulated the mRNA levels of *Alp* by 12 folds on day 3, *Col1a1* by 22 folds on day 3, *Runx2* by 4 folds on day 3, *Alp* by 31 folds on day 5, *Col1a1* by 6 folds on day 5, and *Runx2* by 1.8 folds on day 5, respectively. In comparison with the MAM and SRT groups, MAM/SRT group demonstrated a substantial increase in the expressions of osteoblast-specific genes. To further assess the expressions of OPN, Runx2, β-catenin, acetylated FoxO3a, and SIRT1 proteins, we performed western blotting studies. We found that SIRT1 and β-catenin were significantly upregulated and FoxO3a acetylation were downregulated in both SRT and MAM/SRT groups; that no significant differences were observed in the expressions of SIRT1, acetylated FoxO3a, and β-catenin proteins between SRT and MAM/SRT groups; and that MAM alone did not increase the expression of SIRT1 protein. These findings indicated that MAM/SRT sustainedly released SRT2104 to activate the expression of SIRT1 protein. Similar efficiency of SIRT1 activation was found between MAM/SRT treatment and SRT intermittent treatment. Moreover, as expected, the protein levels of OPN and Runx2 were significantly increased after MAM or SIRT treatment. Of note, MAM/SRT treatment significantly upregulated the levels of OPN and Runx2 compared with MAM treatment or SIRT treatment alone (Fig. 5G). These results indicated that MAM/SRT can sustainedly release SRT and have the ability for promoting osteogenesis as MAM.

ALP staining showed that SRT treatment led to a slight production of ALP in BMSCs while MAM and SRT/MAM groups exhibited much stronger ALP staining, suggesting MAM and SRT/MAM treatments were more effective in stimulating the production of ALP than bolus SRT treatment. Further quantitative measurement of ALP supported these findings and showed that the MAM/SRT increased the expression of ALP by 1.8 folds compared to SRT, indicating that MAM/SRT display more

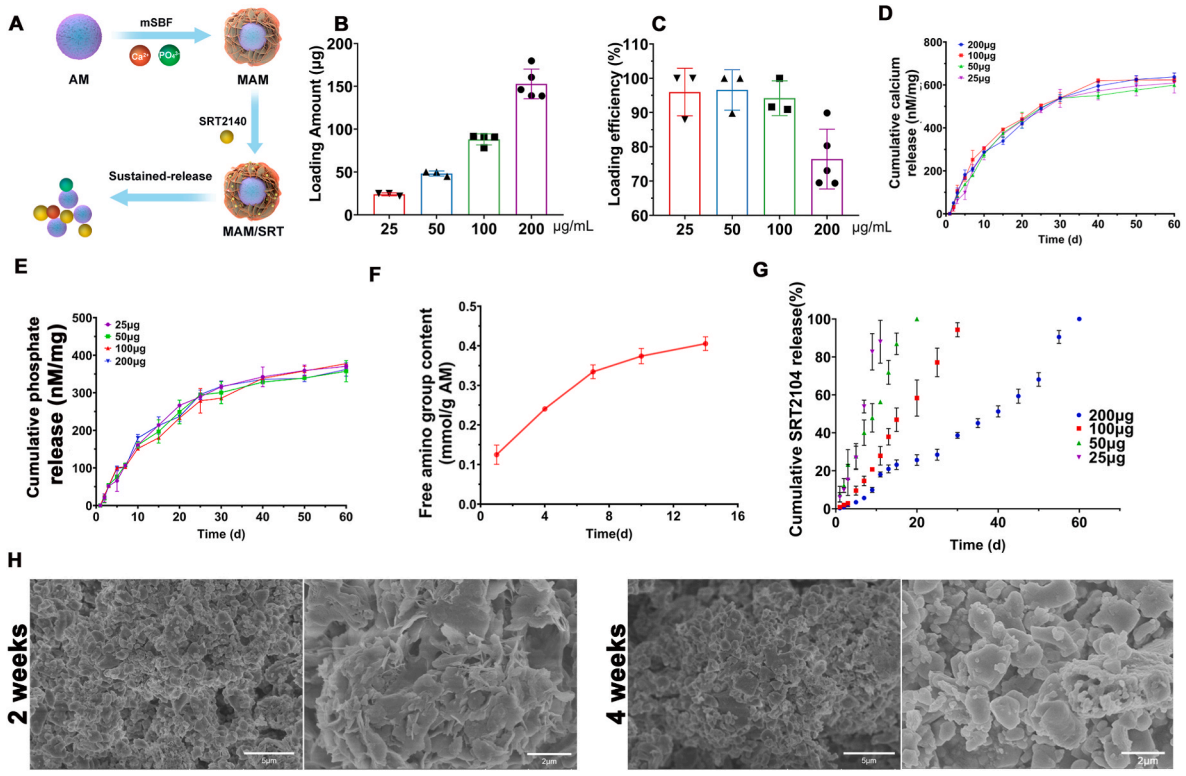

Fig. 3. Binding and sustained release of SRT2104. (A) Brief schematic diagram of MAM/SRT scaffold construction. (B) The amount of SRT2104 loaded on MAM in different concentration of SRT2104 Loading solution. (C) The drug loading efficiency and corresponding drug loading content in MAM/SRT. (D) Cumulative calcium release amount were measured by an Arsenazo III based assay. (E) Cumulative phosphate release amount were measured by an acetone-acid-molybdate based assay. (F) Free amino release amount from AM. (G) Cumulative SRT2104 release percent from various dosage MAM/SRT. (H) The degradation of MAM/SRT were assessed at 2 weeks and 4 weeks by electronic speculum.

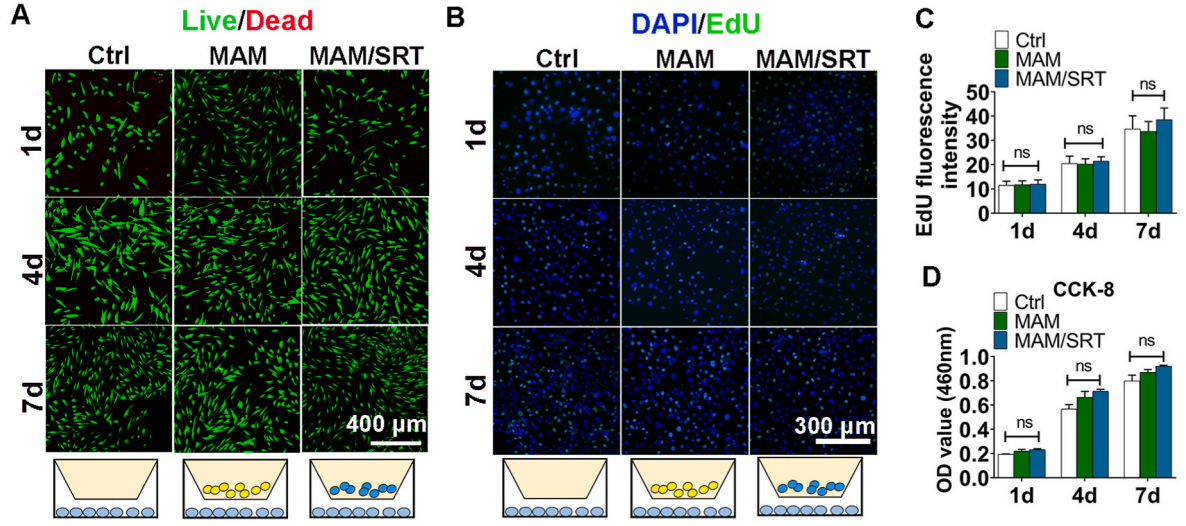

Fig. 4. MAM/SRT did not affect cell proliferation and viability. A, Calcein/PI staining analysis for BMSCs viability. Green fluorescence represents live cells. Red fluorescence represents dead cells. B, EdU fluorescence staining for BMMs proliferation. Green fluorescence represents proliferating cells. Blue fluorescence represents cellular nucleus. C, the quantitive analysis of EdU fluorescence staining. Sham, cells were treated with 0.1% DMSO using transwell insert. MAM, cells were treated with 1 mg MAM using transwell insert. MAM/SRT group, cells were treated with 1 mg MAM/SRT (10 mg/100 μg/mL) using transwell insert; ns represents no significant difference. D, CCK-8 assay for BMSCs viability. Data are expressed as the mean ± standard deviation (SD) (n = 3); ns represents no significant difference.

excellent capability in osteogenesis than MAM or SRT alone (Fig. 4G and H). Furthermore, mineral deposits are the mature marker of osteogenic differentiation of BMSCs [19]. The mineral deposits were also examined by Alizarin Red staining at day 12 after osteogenic induction (Fig. 5J). The sham group showed a few nodules stained in red whereas the MAM, SRT, and MAM/SRT groups showed more than sham group. Cells treated with MAM/SRT showed strong positive red mineralized nodules. The quantitative analysis of mineralized nodule also presented that MAM/SRT group displayed a 2.74-fold increase compared with SRT group, and a 1.95-fold increase compared with MAM group. MAM/SRT

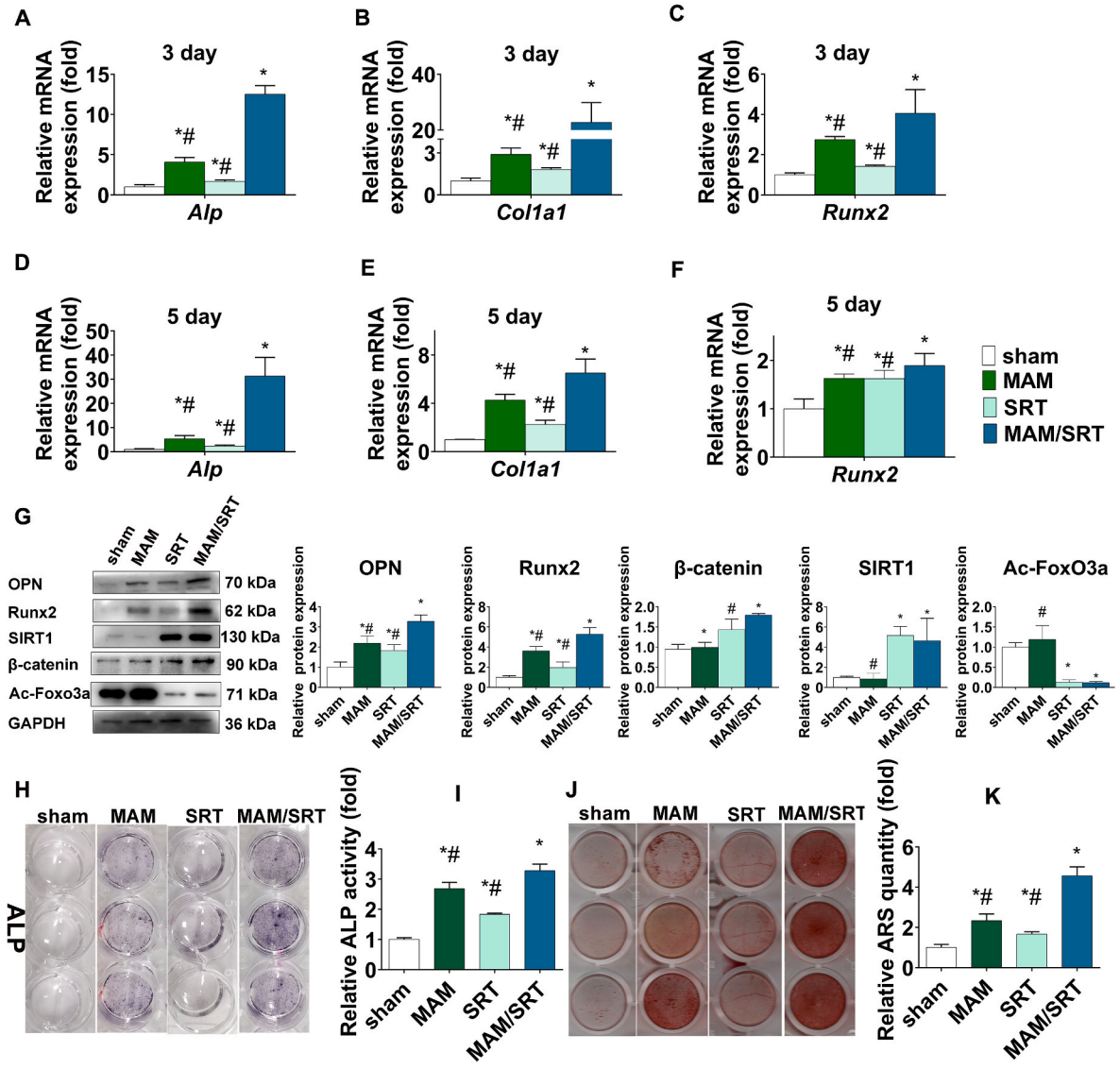

Fig. 5. MAM/SRT enhanced osteogenic differentiation of BMSCs. (A–C) *Alp*, *Col1a1*, and *Runx2* mRNA were analyzed by RT-qPCR at day 3 after osteogenic induction. (D–F) *Alp*, *Col1a1*, and *Runx2* mRNA were analyzed by RT-qPCR at day 5 after osteogenic induction. (G) Expression levels of SIRT1, RUNX2, OPN, acetylated FoxO3a (Ac-FoxO3a), and β-catenin were determined by WB analysis at day 3 of osteogenic differentiation. Protein expression levels were normalized to glyceraldehyde-3-phosphate dehydrogenase (GAPDH). Data are expressed as the mean ± SD of three independent experiments, and one of three independent experiments is shown. $^{*}p < 0.05$ vs. BMSCs in sham group. (H), Alkaline phosphatase staining was determined at day 3 of osteogenic differentiation of BMSCs. (I), Alkaline phosphatase activity was determined at day 3 of osteogenic differentiation of BMSCs. Data are expressed as the mean ± SD of three independent experiments, and one of three independent experiments is shown. $^{*}p < 0.05$ vs. BMSCs in sham group. $^{\#}p < 0.05$ vs. BMSCs in MAM/SRT group. (J), Mineral deposits were determined by Alizarin Red staining at day 12 after osteogenic induction. (K) The quantitative analysis for Alizarin Red staining at day 12 after osteogenic induction. $^{*}p < 0.05$ vs. BMSCs in sham group. $\#p < 0.05$ vs. BMSCs in MAM/SRT group.

displayed the strongest mineralization ability, which revealed that the synergistic effects of MAM and SRT2104 offered a more efficient way to increase bone formation.

4. MAM/SRT decreased the osteoclastogenesis

Next, the effects of MAM/SRT on osteoclastogenesis were investigated using bone marrow–derived monocytes (BMMs) *in vitro*. Osteoclasts are typically characterized by multinucleated and tartrate-resistant acid phosphatase (TRAP)-positive cells. TRAP staining showed that significantly less osteoclasts were observed in SRT and MAM/SRT groups after osteoclastic differentiation on day 5 than these in both MAM and sham group (Fig. 6A).

Osteoclast bone resorption function requires an extensive F-actin reorganization [20]. To adhere to the surface of the mineralized matrix, changes in osteoclast morphology are induced by organizing cytoskeletal F-actin into a specific structure. The osteoclasts can establish an acidic microenvironment by F-actin between extracellular matrix and its ruffled border that has prominent subdomains for osteolysis [21]. Compared with sham group, MAM group had no significant effect in the formation of F-actin rings. F-actin rings were smaller in the MAM/SRT group and SRT group (Fig. 6B). The quantitative analysis of the size of F-actin rings also revealed that the decreased F-actin formation ability of groups containing SRT2104 was significantly higher than that of other groups, but there were no significant differences between MAM/SRT and SRT group, while MAM group displayed no effect in F-actin ring formation.

Further, bone resorption pit assays were carried out to assess the role of MAM/SRT on the function of osteoclasts. Similarly, no significant difference in the number and the size of bone resorption pits were

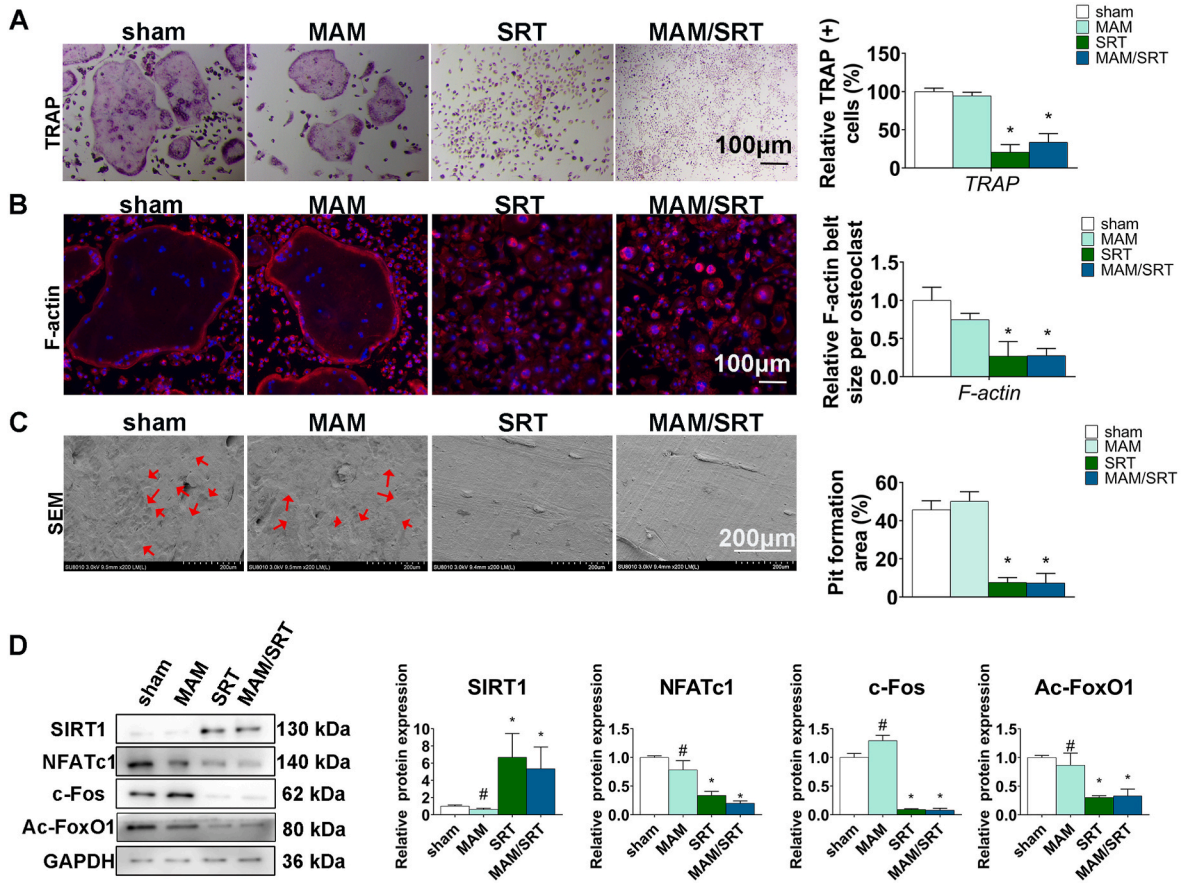

Fig. 6. MAM/SRT suppressed the osteoclastogenesis in vitro. (A) TRAP staining for osteoclasts formation at day 5 after osteoclastic induction. Scale bars = 100 μm $^{*}p < 0.05$ vs. sham group. $^{\#}p < 0.05$ vs. MAM/SRT group. (B) Immunofluorescence for RANKL-induced F-actin ring formation *in vitro*. The average F-actin belt size were normalized with sham group. Red represents F-actin labeling with phalloidin and blue represents the nucleus stained with DAPI. Scale bars = 100 μm $^{*}p <$ 0.05 vs. sham group. $^{\#}$P < 0.05 vs. MAM/SRT group. (C) Scanning electron microscope for bone resorption pits by osteoclasts. Scale bars = 200 μm $^{*}p < 0.05$ vs. sham group. $^{\#}p < 0.05$ vs. MAM/SRT group. (D) Expression levels of SIRT1, NFATc1, c-Fos and acetylated FoxO1 (Ac-FoxO1) were determined by WB analysis at day 3 of osteoclastic differentiation. Protein expression levels were normalized to glyceraldehyde-3-phosphate dehydrogenase (GAPDH). Data are expressed as the mean ± SD of three independent experiments, and one of three independent experiments is shown. $^{*}p < 0.05$ vs. sham group. $^{\#}p < 0.05$ vs. MAM/SRT group.

obtained between sham and MAM groups. MAM/SRT or SRT treatment significantly decreased the number and the size of bone resorption pits compared with AM treatment. The quantitative analysis showed a 78% reduction in SRT group and a 74% decrease in MAM/SRT group, while no significantly difference was observed between the MAM/SRT group and SRT groups (Fig. 6C).

The osteoclast-specific proteins were further also examined by Western blot analysis. Osteoclast-specific markers include *TRAP, MMP-9, cathepsin K, NFATc1, ATPase,* and *c-Fos* [22]. Following receptor activator of nuclear factor-κB (NF-κB) ligand (RANKL) induction, *c-Fos* binds to the *NFATc1* promoter to induce auto-amplification during osteoclast differentiation [23]. NFATc1 is considered as a master transcription factor that regulates the expression of osteoclast-specific genes such as MMP-9, TRAP, cathepsin K, and ATPase [24]. The results revealed that the presence of MAM/SRT or SRT significantly increased the levels of SIRT1. The protein levels of SIRT1 was 5.1-fold upregulated in SRT group, and 4.6-fold increase in MAM/SRT group. However, no significantly difference was detected between SRT and MAM/SRT group. A 92% relative decline in c-Fos, an 80% reduction in NFATc1 and a 67% relative decline in acetylated FoxO1 were found in MAM/SRT group compared with those in sham group. There was a 91% relative decline in c-Fos, a 77% decrease in NFATc1 and a 70% reduction in acetylated FoxO1 due to the SRT treatment. No statistically significant findings were obtained between SRT group and MAM/SRT group (Fig. 6D). Compared with the MAM/SRT group, the upregulation of SIRT1 and the downregulation of NFATc1, acetylated FoxO1, and c-Fos proteins were found after the treatment of MAM.

Excessive activation of osteoclasts induces bone mass loss and results in compromised bone healing. Monocytes differentiate into osteoclasts upon stimulation by macrophage colony-stimulating factor (M-CSF) and RANKL [25]. RANKL binds to RANK on the surfaces of osteoclasts and osteoclastic precursors to promote the differentiation and function of osteoclasts [26]. The difficulties of osteoporotic bone healing result from the imbalanced activity between osteogenesis and osteoclastogenesis. Excessive osteoclastogenesis and abnormal osteoclast activity will certainly result in compromised bone healing or malunion. SRT2104, a highly selective small molecule activator of SIRT1, alleviates the balance disruption caused by excessive bone resorption and declined bone formation [6]. Consistently, we found that intermittent administration of SIRT2104 could inhibit RANKL-induced TRAP positive cells formation, osteoclast-specific protein expression, F-actin ring formation, and bone resorption pit formation *in vitro* [10]. Moreover, these effects on inhibiting osteoclastogenesis were also achieved by MAM/SRT treatment. However, MAM had no effect on the osteoclastogenesis. Thus, we infer that a steady and sustained release of SRT2104 can be achieved by MAM/SRT to decrease excessive osteoclastogenesis.

5. MAM/SRT accelerated the bone healing of osteoporotic defect in rats

To investigate the impact of MAM/SRT on local osteogenesis *in vivo*, an osteoporotic femoral defect was established according to previous studies [27–29]. Osteoporotic status was successfully induced by bilateral ovariectomy and tubal ligation using a dorsal approach (Supplemental Fig. 2). In addition, the bone healing capability is significantly delayed due to osteoporosis. After 6 weeks, a hole (3 mm in diameter and 3 mm in depth) was then produced in distal femur and injected with saline, MAM, or MAM/SRT, and the specimens were collected in 3 and 5 weeks (Fig. 7A).

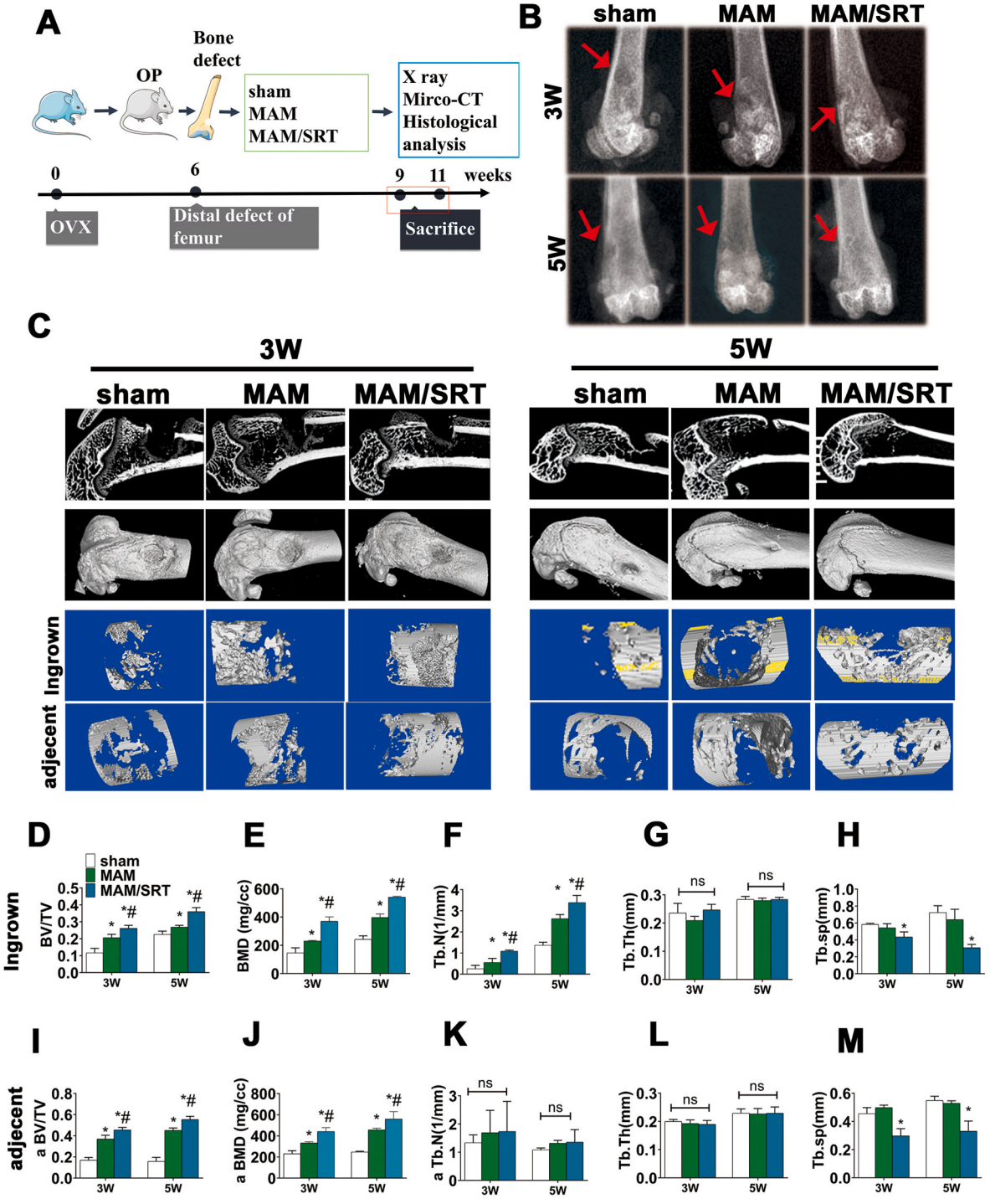

Fig. 7. MAM/SRT accelerated the local bone healing of osteoporotic defect in rats. (A) Schematic for animal experiment. (B) X ray for bone healing after operation on weeks 3 and 5 *in vivo*. Red arrow represents defect area. (C) Microcomputed tomography (micro-CT) analysis of bone healing. (D–H) Bone mineral density (BMD), bone tissue volume/total tissue volume (BV/TV), trabecular number (Tb·N), trabecular thickness (Tb·Th), and trabecular separation (Tb.Sp) of ingrown bone tissue were assessed using micro-CT quantitatively analysis. (I–M) Bone mineral density (BMD), bone tissue volume/total tissue volume (BV/TV), trabecular number (Tb·N), trabecular thickness (Tb·Th), and trabecular separation (Tb.Sp) of the adjacent bone tissue were assessed using micro-CT quantitatively analysis. Data are expressed as the mean ± SD of three independent experiments, and one of three independent experiments is shown. $^{*}p < 0.05$ vs. sham group. $^{\#}p < 0.05$ vs. AM group.

X ray and micro-CT were performed to assess the bone defect healing. The representative images of X ray were shown in Fig. 7B. Bone defects were pointed out in red arrows. There were clear margins to adjacent normal cortical and cancellous bones in sham group at 3 weeks. The margin of the initial circular defects was not clearly identifiable in MAM and MAM/SRT group at 3 weeks. The margins of the bone defects were indistinct in sham group at 5 weeks. MAM group exhibited some bone regenerations but a significantly bone defect at 5 weeks, while the femoral bone defect is basically healed in MAM/SRT group. The healing speeds of bone defect in MAM group and MAM/SRT group were accelerated compared with those in sham group (Fig. 7B).

Further, quantitative assessment of micro-CT was performed. The images of micro-CT were presented in Fig. 7C and D. As expected, the results were consistent with those of X ray. At 3 weeks after surgery, the bone defect in the sham group was still empty. There was a certain extent of improvement in bone regeneration in MAM group. Of note, MAM/SRT group had more calluses than the other groups. The results of micro-CT at 5 weeks after surgery were similar with these at 3 weeks. As shown in Fig. 7C, the sham group had some degree of bone healing. In the MAM group, the density of callus tended to be uniform and the bone defect was completely repaired due to residual small cortical bone defect. To be gratified, the newly formed bone was integrated well without obvious boundary and the bone defect healed completely in the MAM/SRT group. According to a previous study [30], bone mineral density (BMD), bone tissue volume/total tissue volume (BV/TV), trabecular thickness (Tb·Th) and trabecular number (Tb·N), trabecular separation (Tb.Sp) were quantitatively assessed in bone defect areas (Fig. 4D–H) and bone defect adjacent bone areas (Fig. 4I-M). The MAM group exhibited significantly higher BMD (230.33 ± 4.77 mg/cm^3 vs. 146.06 ± 36.28 mg/cm^3), BV/TV (0.23 ± 0.02 vs. 0.12 ± 0.03), and Tb·N (0.55 ± 0.15/mm vs. 0.26 ± 0.12/mm) than the sham group at postoperative 3 weeks. Similar results were detected at postoperative 5 weeks. Higher BMD, BV/TV, and Tb·N were in MAM group than those in sham group. BMD, BV/TV and Tb·N of the newly formed bones in MAM/SRT group were highest among these three groups. Similar trends were obtained in defect adjacent bone areas. From 3 to 5 weeks, the BV/TV and BMD in sham group did not significant change, while those in MAM/SRT and MAM groups significant increased. At week 3, the BV/TV of the MAM/SRT group was 2.7- and 1.2-fold significantly higher than that of the sham and MAM groups, respectively. BMD and Tb·N in MAM/SRT were also higher than those in other groups. At week 5, Higher BMD (560.05 ± 69.92 mg/cm^3 vs. 456.97 ± 16.08 mg/cm^3) and BV/TV (0.55 ± 0.03 vs. 0.452 ± 0.02) were observed in MAM/SRT than those in MAM group. Significantly decreased trabecular separation (Th. Sp) were observed in MAM/SRT group. The above-mentioned results suggested that MAM and MAM/SRT treatment can enhance bone density of defect to promote bone regeneration and osteointegration.

Histological examination, including HE staining and TRAP staining were performed to assess the healing of osteoporotic bone defects. At postoperatively 3 weeks, HE staining displayed that the defect sites (green circle) were filled with substantial fibroblasts and adjacent bone area were without callus formation (red square) in the sham group (Fig. 8A). The defect area appeared some continuous new bone tissue and adjacent bone area displayed a certain density of the trabeculae bone (red square) in the MAM group. Whereas, MAM/SRT resulted in substantial new bone formation in defect areas and trabeculae bones filled with adjacent bone area (Fig. 8A). At postoperative 5 weeks, substantial fibroblasts and minor trabeculae bone were found in the defect sites and scarce new bone formation were in junctional zone in sham group. The defect areas of MAM group significantly newly formed bone tissue were clearly observed, and prior adjacent bone areas were healing. Notably, the bone defect was found to be healed completely in the MAM/SRT group, filled with regenerated bone tissue and integrated with surrounding bone seamlessly (Fig. 8B).

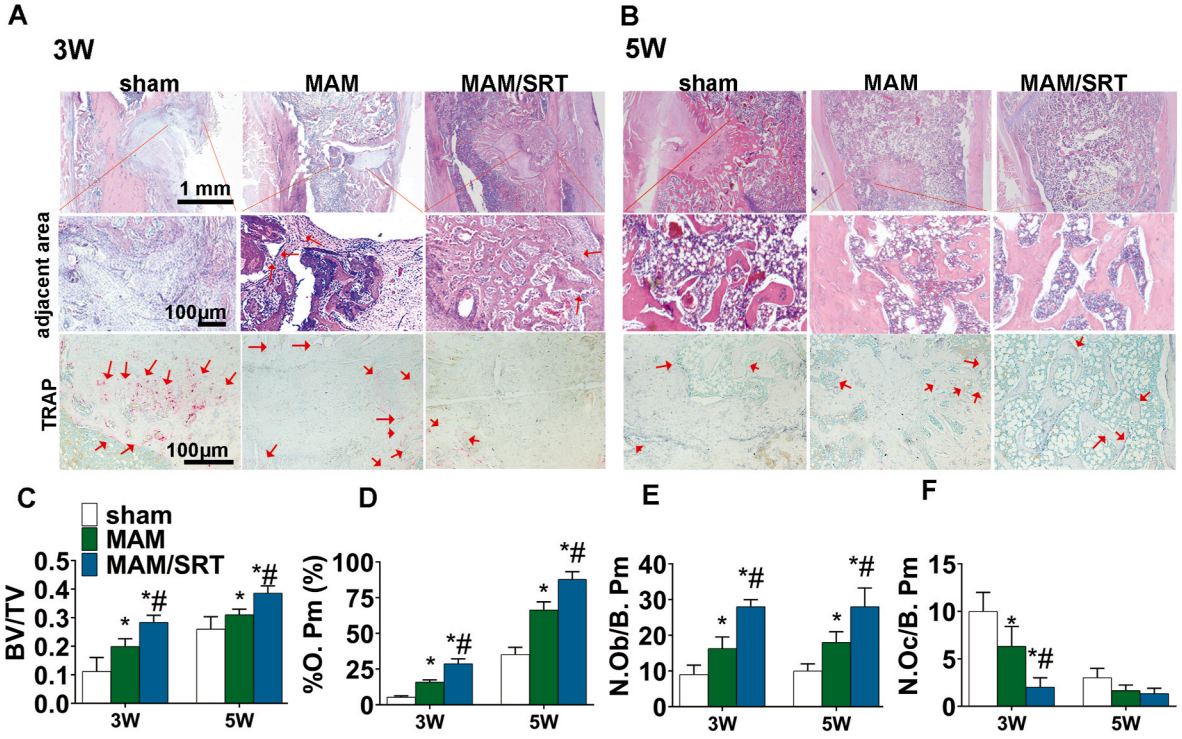

Fig. 8. MAM/SRT speeded osteoporotic bone healing, increase surrounding bone density and decreased the excessive osteoclastogenesis. (A) HE staining and TRAP staining of defect area at the third postoperative week. (B) HE staining and TRAP staining of defect area at the fifth postoperative week. (C) Bone tissue volume/total tissue volume (BV/TV). (D) Osteoblast number (N.Ob/B. Pm) in the bone defect healing area. N. Ob/B.Pm = osteoblast number/bone perimeter. (E) The percent of Osteoid perimeter (%O. Pm) in the bone defect healing area. (F) Osteoclast number (N.Oc/B. Pm) in bone defect healing area. N. Oc/B.Pm = osteoclast number/bone perimeter. Data are expressed as the mean ± SD of three independent experiments, and one of three independent experiments is shown. *$p < 0.05$ vs. sham group. $^{\#}p < 0.05$ vs. MAM group.

Moreover, according to previous studies [1–3], the pathological parameters reflecting bone formation [BV/TV, Osteoblast number (N. Ob/B. Pm), the percent of Osteoid perimeter (%O. Pm)] and bone resorption [Osteoclast number (N.Oc/B. Pm)] were examined. HE staining of the bone defect areas, showed that MAM group exhibited significantly more bone formation compared with sham group. Histomorphometric analyses confirmed that the highest BV/TV was observed in MAM/SRT group (0.283 ± 0.020 at postoperative 3 weeks, 0.387 ± 0.021% at postoperative 5 weeks) than other groups (Fig. 8C). Higher percentage of osteoid perimeter (% O. Pm) (65.83 ± 6.85% vs. 45.30 ± 7.90%) and more osteoblast numbers (N.Ob/B. Pm) (28.00 ± 1.00 vs. 16.33 ± 3.00) were observed in MAM/SRT than those in MAM group at postoperative 3 weeks (Fig. 8D and E). Similar results were also detected at postoperative 5 weeks (Fig. 8D and E). The TRAP staining was also carried out to demonstrate the role of MAM/SRT on the osteoclast activity *in vivo*. The results showed that MAM/SRT decreased excessive osteoclastogenesis (red areas) in adjacent bone areas at postoperatively 3 weeks (Fig. 8A, F), which indicates that MAM/SRT treatment can prevent excessive bone loss to enhance osseointegration by inhibiting osteoclastogenesis. However, no significantly difference was found among those three groups at postoperatively 5 weeks (Fig. 8A, F). OPN levels were also assessed using immunohistochemistry (IHC) in bone tissue sections. The highest levels of OPN staining were observed in MAM/SRT group than the other groups at 3 or 5 weeks (Supplemental Fig. 5), which suggests that MAM/SRT exerted synergistic effects on new bone formation. Overall, our MAM/SRT delivery system served as a high efficient bone homeostasis regulator to accelerate osteoporotic bone healing and increase surrounding bone density to provide enough bone strength.

In this study, we developed a SIRT-1 agonist delivery system to locally reverse the imbalanced bone homeostasis under osteoporotic condition. SRT2104 was firmly immobilized on the mineral coating formed on acellular matrix microparticles. The mineral coating interacts with the surrounding environment and degrades concurrently with SRT2104 release for over 30 days *in vitro* (Fig. 3). The release of SRT2104 exhibited near zero-order release kinetics without a "burst" release (Fig. 3F). Moreover, the drug loading efficiency and corresponding drug loading content in this release system were highly effective. Therefore, the cells in bone defect received continuous, sufficient, and steady stimulation to promote bone healing. Decreased pore size were observed in MAM/SRT due to mineral coating (Fig. 2E and Supplemental Fig. 1). The smaller pore size of the mineral coatings may be able to enable more sustained release of bioactive molecules [12]. Moreover, the local sustained release of SRT2104 not only upregulated the activities of β-catenin and Runx2 to enhance osteogenic differentiation of BMSCs and mineralization (Fig. 5), but also mediated the expressions of deacetylated FoxO1 and NFATc1 to suppress osteoclastogenesis and osteoclast activity (Fig. 6). Moreover, the application of MAM/SRT remarkably increased healing speed of osteoporotic defect compared with MAM implant (Figs. 7 and 8). Collectively, our MAM/SRT system effectively reversed the imbalance under osteoporotic pathological conditions and led to enhanced bone formation and decreased aberrant bone resorption.

SIRT1 with versatile roles enabled simultaneous regulation of multiple signaling pathways to tackle osteoporosis, which is superior to most current clinical approaches targeting a single specific pathway. Currently, the most used clinical anti-osteoporotic drugs function either by inhibiting bone resorption or enhancing bone formation, however the bone repair of osteoporosis sites is particularly difficult due to the deficient bone forming ability and excessive bone resorption. Unlike previous treatments, SIRT1 is capable of integrating multiple upstream signals to promote osteoblastogenesis and to inhibit osteoclastogenesis by regulating multiple downstream targets, including the stimulation of β-catenin, FOXOs and Runx2 and the negative regulation of NFκB and PPARγ [7]. As an upgraded highly-effective small molecule agonist for SIRT1, the sustained-release of SRT2104 provided a vital upstream signal to regulate multiple signaling pathways. In addition, SIRT1, an NAD + -dependent deacetylase, can deacetylate histone and non-histone substrates, including P53 and FOXOs [31,32]. In our study, MAM/SRT enhanced osteogenic differentiation of BMSCs and mineralization by SIRT1/β-catenin, SIRT1/Runx2, and SIRT1/deacetylated FoxO3a signaling cascades (Fig. 5). Notably, Wnt/β-catenin signaling, Runx2 transcription, and FoxO3a deacetylation are currently considered the master mediators of osteogenesis and bone formation [32–34]. Moreover, we found that the sustained-release of SRT2104 by MAM/SRT had the same effect as intermittent administration of SIRT2104 to alleviate osteoclastogenesis and bone resorption (Fig. 6). Similar to previous studies [6,35], the activation of SIRT1 inhibited osteoclast formation and activity by deacetylating FoxO1 and thereby downregulating the expressions of NFATc1 and c-Fos. In addition, OVX-induced osteoporosis model also validated that MAM/SRT speeded bone healing, improved bone quality and suppressed excessive osteoclasts (Figs. 7 and 8), which indicated that the sustained-release of SRT2104 by this delivery system exerted a dual-regulatory effect to enhance bone formation and inhibited excessive bone resorption.

In this delivery system, a bone-like mineral coating formed using mSBF was employed as carriers for a small molecule drug for the controlled release. The release of drug was sustained for more than one month *in vitro*. Conventionally, SRT2104 was administrated via oral or intravenous route, similar to most small molecule drugs. However, its efficacy and targeted distribution to bone tissue are considered to be low. Binding of small molecule drug with the mineral coating improves the efficiency and reduces the adverse effects. The small molecule drug was firmly immobilized onto the mineral coating, and gradually released to fulfill their role during bone healing. We found that such sustained release mode of SRT2104 showed significantly higher efficacy compared to bolus addition of the molecule into the medium (Fig. 6). In addition, various of bioactive components such as collagen, polypeptide, calcium ions were released into the microenvironment of bone healing during MAM degradation, which might play beneficial role in promoting bone formation as these components are known to be the building blocks of new bone [36].

These *in vitro* and *in vivo* data together suggest that MAM/SRT can sustainedly release SIRT2104 and displayed a synergistic effect with MAM. It exerts the dual effects of simultaneously regulating osteogenesis and osteoclastogenesis via integrating multiple vital upstream signals. Of note, this is just a preliminary result, which remains to be further confirmed by large-animal or clinical researches. Overall, MAM/SRT capable of releasing SRT2104 in a sustained manner might be a promising approach for osteoporotic bone healing.

6. Materials and methods

6.1. Reagents and mice

Acellular matrix microparticles (AM) were obtained from porcine acellular dermal matrix [15]. Chemicals for preparing modified simulated body fluid (mSBF) were purchased from Sigma Chemical Co. (USA). This study was carried out in accordance with the principles of the Basel Declaration and the recommendations of Zhejiang University. The protocol was approved by the Animal Ethics Committee of Zhejiang University (No.2021065). BMSCs and BMMs isolated from 10-week-old C57BL/6 mouse (Slack, Shanghai, China).

6.2. Acellular matrix microparticles (AM) preparation

Acellular matrix microparticles (AM) were prepared by decellularization of the porcine dermis as our previously described [15]. Briefly, the porcine dermis was cut into strips, washed with de-ionized water and 0.2% peracetic acid for 2 h. Immediately after, the dermis was milled to microfibrous in saline, and added into a series of solutions for decellularization: (1) 24 mM sodium deoxycholate + 0.2% EDTA for 1 day with

continuous agitation, (2) 0.9% NaCl solution for 15 rinse-centrifuge cycles.

6.3. DNA and fat residue measure

The methods were consistent with our previously described [15,37]. To detect the DNA residue of AM, the DNA was extracted using the DNeasy Blood & Tissue Kit (QIAGEN). Then, the DNA was analyzed using PicoGreen dsDNA assay kit (Invitrogen). The fluorescence of each sample was read at Ex/Em of 485/530 nm and evaluated the residue DNA.

For fat residue quantification, firstly, AM was hydrolyzed with 6 M HCl at 80 °C. Thereafter, the fat was extracted with anhydrous ether and oven drying to a constant weight; the weight of residue fat was quantified by using analytical scale (Mettler Toledo, United States).

6.4. Collagen content determination

The collagen content was analyzed through determining the amount of hydroproline (HYP) [37]. Briefly, AM was incubated with 6 M HCl in an oven at 105 °C overnight. After hydrolysis, the sample was adjusted to neutral pH and oxidized with chloramine-T. Next, the sample was added to p-dimethylaminobenzaldehyde at 60 °C for 20 min. Finally, the HYP concentration was measured at 560 nm using a microplate reader (Mettler Toledo, United States).

6.5. Free amino group content determination

Firstly, the supernatants of AM were diluted 10 folds, and 50 μL of 0.01% (w/v) 2,4,6-trinitrobenzene sulfonic acid (TNBS) solution were incubated with 100 μL aliquots of the diluted solutions. Then, the mixture was shielded from light and was incubated in a temperature-controlled water bath at 40 °C for 2 h. The reaction was terminated with 50 μL of 10% (w/v) SDS. The absorbance at 335 nm was measured, and the free amino group content was calculated from a standard curve [38].

6.6. Mineral acellular matrix microparticles (MAM) preparation

The acellular matrix microparticles were coated with a layer of mineral coating by incubating in modified simulated body fluid (mSBF) at 37 °C for 7 days with continuous rotation (100 rpm/min). The mSBF was prepared as our previously reported [13]. Specifically, the following reagents were added to deionized water in the order shown: 141 mM NaCl, 4.0 mM KCl, 0.5 mM $MgSO_4$, 1.0 mM $MgCl_2$, 20.0 mM HEPES, 5.0 mM $CaCl_2$, 2.0 mM KH_2PO_4, and 4.2 mM $NaHCO_3$. The pH of mSBF was then adjusted to 6.80 by adding HCl/NaOH solution. Each 1 g acellular matrix microparticles were incubated in 50 mL mSBF in a conical tube with mSBF being refreshed daily to maintain consistent calcium and phosphate ion concentrations for continued coating growth. The resultant AM were washed in deionized water and lyophilized prior to characterization.

6.7. AM characterization

The morphology and composition of AM were examined by scanning electron microscopy (SEM), X-ray diffraction (XRD), and Fourier transform infrared (FTIR) spectroscopy. Morphological and elemental analysis was carried out using a field emission scanning electron microscope (FE-SEM, SU-8010; Hitachi, Kotyo, Japan) at an accelerating voltage of 3 kV. Prior to characterization, the samples were added directly on top of conductive tapes and sputter-coated with gold for 60 s. The energy-dispersive spectroscopy (EDS) system was used for calculating the Ca/P ratio. The phase composition of the mineral coating was identified with X-ray diffractometer (XRD, D8 Advance; Bruke, Germany) with CuKα radiation. The composition of the AMs and MAMs was analyzed via Fourier transform infrared spectroscopy (FTIR, Nicolet 10; Thermo scientific, USA). For each measurement, 128 scans were obtained with a resolution of 4 cm-1, with wavelengths ranged from 400 to 4000 cm-1.

6.8. Binding and release of SRT2104 from MAM

Each 10 mg AM was immersed in 1 mL PBS solutions containing four kinds of SRT2104 concentrations (25, 50, 100, and 200 μg/mL) at 37 °C for 2 h with rotation to allow for binding. After binding, the drug-loaded AMs were then centrifuged at 12000 RPM for 2 min and washed with PBS once, and the amount of SRT2104 in the supernatant was determined by measuring absorbance at 330 nm using microplate reader. The concentration was calculated by a set of standards with predetermined drug concentrations. The binding efficiency of each group was calculated from the SRT2104 concentration change before and after binding.

After rinsing, each group of SRT2104-loaded AMs was incubated in 1 mL of SBF (pH 7.4) at constant 37 °C with rotation. At predetermined time point, 1 mL of release medium was withdrawn by centrifugation and an equal volume of medium was replenished. The release amount of SRT2104 was determined by microplate reader at the wavelength of 330 nm (Supplemental Fig. 4). The release tests were performed in triplicate.

6.9. Dissolution of MAM

The stability of MAM was evaluated by calculating the amount of calcium and phosphate released into simulated body fluid (SBF, pH 7.40). Briefly, each 10 mg of AM was incubated in 1.0 mL SBF in a 1.5 mL Eppendorf tube at 37 °C with continuous rotation. At various predetermined time points, 1 mL of SBF releasing medium was collected from the tube and an equal volume of fresh SBF was replenished. The amount of calcium was quantified by an Arsenazo III based assay. Briefly, 5 μL of sample was mixed with 195 μL of 0.4 mM Arsenazo III in 20 mM Tris buffer (pH 7.40). The amount of calcium was determined by measuring absorbance at 615 nm using microplate reader, and the concentration was calculated by a set of standards with predetermined calcium concentrations. The phosphate amount released was quantified by an acetone-acid-molybdate (AAM) based assay [16]. In brief, 100 μL of releasing buffer was blended with an equivalent volume of AAM solution containing 10 mM ammonium molybdate, 5.0 N sulfuric acid, and acetone. The amount of phosphate was determined by measuring absorbance at 405 nm, and the concentrations were also calculated by a series of predetermined phosphate standards. All data were normalized to the mass of the sample. After a 60-day incubation the samples were washed with deionized water and freeze dried, and the morphology was examined by SEM.

6.10. Cell proliferation and viability assay

To assess the effects of materials on cell proliferation and viability, Cell Counting Kit-8 (CCK8), Calcein/PI staining, and EdU fluorescence analysis were performed.

For CCK8, BMSCs were supplemented with 10% CCK8 (Dojindo, Kumamoto, Japan) in low-glucose Dulbecco's Modified Eagle's Medium for 120 min in 5% CO_2 at 37 °C. Absorbance at 450 nm was measured using a microplate reader (ELX808; BioTek, Winooski, VT, USA).

For Calcein/PI cell viability assay, after pretreatment, live BMSCs and dead BMSCs were detected using Calcein/PI assay kit (Beyotime, Shanghai, China) in accordance with the manufacturer's protocols.

For EdU staining, following treatment, BMMs viability were investigated using an EdU kit (Beyotime, Shanghai, China) in accordance with the manufacturer's protocols.

6.11. BMSCs isolation and osteoblastic differentiation

Mouse BMSCs were isolated in accordance with previous study [39].

A syringe needle was inserted into the bone marrow cavity and the marrow was flushed out with α-MEM medium. Later, the long bones were cut into 1 mm^3 chips. The bone chips were digested with collagenase type II for 1 h in a shaking incubator at 37 °C with a shaking speed of 200 rpm. After that, bone chips were cultured in α-MEM with 10% FBS. After 5 day in culture, harvested BMSCs and passaged. The cells (3×10^4 cells/cm^2) were seeded into 24-well plates. Two days later, BMSCs were induced by osteogenic induction medium every 3 days in accordance with our previous studies [19,34,40]. The materials were sterilized by ethylene oxide prior to use. Transwell inserts were placed in the 24 well-plate to separate the material from the cells.

6.12. Alizarin red staining and quantification

Alizarin Red staining were performed to assess mineral deposition. After induction, cells were fixed with 4% paraformaldehyde for 20 min and washed gently 3 times. The cells were incubated with a 1% alizarin red solution. The Alizarin Red stain was eluted with 10% cetylpyridinium chloride for 15 min and was measured at an OD of 570 nm for quantification using a microplate reader (ELX808, BioTek) [37,41].

6.13. ALP staining and activity assay

The methods were consistent with the method of our previous studies [34,40,42,43]. For ALP staining, cells were fixed with 4% paraformaldehyde for 20 min and washed gently 3 times. Fixed cells were stained with an ALP Staining Kit (Beyotime, Shanghai, China).

For ALP activity assay, briefly, cells were lysed. Then, the lysate was mixed with fresh solution containing the substrate p-nitrophenyl phosphate for 30 min. The reaction was interrupted by NaOH, and absorbance was measured at 405 nm using an ELX800 absorbance microplate reader.

6.14. BMM isolation and osteoclast differentiation

According to our pervious study [43], BMMs were isolated from long bones of 10-week-old C57BL/6 mouse (Slack, Shanghai, China). Cells were cultured in α-MEM supplemented with 10% FBS and 30 ng/mL M-CSF. Immediately after, BMMs were (8×10^3 cells/well) were seeded into 96-well plates and cultured with M-CSF (30 ng/mL), RANKL (100 ng/mL) and for 4–6 days until the formation of osteoclasts. Next, cells were fixed with 4% paraformaldehyde and stained with a TRAP staining kit (42010102, Shanghai, Sigma-Aldrich). TRAP-positive cells with five or more nuclei were considered as mature osteoclasts, which were counted and quantified.

6.15. Phalloidin staining assay

Phalloidin Staining was carried out according to the manufacturer's instructions (Invitrogen, Shanghai, China). Treated cells were fixed with 4% paraformaldehyde, permeabilized with 0.1% Triton X-100 and stained with rhodamine-conjugated phalloidin (1:200, diluted in 2% BSA in PBS; Invitrogen) for 1 h at 37 °C. Immediately after, the nuclei were stained with DAPI. Fluorescent photographs were obtained using a fluorescence microscope (Leica, Germany). F-actin belt were quantified using ImageJ software.

6.16. Bone resorption assay

According to our previous study [43], sterile bovine bone slices were placed in the 96-well plates, and then BMMs (1×10^4 cells/well) were seeded on the bovine bone slices. Following induction of osteoclast differentiation for 8 days, the bone resorption on bone slices were observed and captured by the scanning electron microscope (HITACHI, Tokyo, Japan).

6.17. Serum PINP level assay

Serum pro-collagen type 1N-terminal peptide (P1NP) levels were evaluated at 6 weeks after OVX modeling by an ELISA kit (MyBioSource Inc., San Diego, CA, USA). The experiment was performed as previous study [44].

6.18. RT-qPCR

Total cellular RNA was isolated and reverse-transcribed into cDNA according to our previous study [34] All gene transcripts were quantified by PCR using the Power SYBR® Green PCR Master Mix (Takara Bio, Kusatsu, Japan) on the ABI StepOnePlus System (Applied Biosystems, Warrington, UK). mRNAs of the target genes and the housekeeping gene (glyceraldehyde 3-phosphate dehydrogenase [*GAPDH*]) were quantified in separate tubes. All primers were synthesized by Sangon Biotech. The PCR conditions were as our previous studies [40]. All primers information is listed in Table 1.

6.19. Western blot analysis

Following treatment, Western blot analysis was carried out in accordance with our previous studies [40,43]. Briefly, proteins were collected and quantified. Next, they were separated and then transferred to a polyvinylidene fluoride membrane. After above steps, the membranes were incubated with primary antibody and corresponding second antibody. After exposure, the immunoreactive bands were detected. All antibodies information is listed in Table 2.

6.20. In vivo evaluation of rats

All experiments were conducted in accordance with the Animal Care and Use Committee guidelines of Zhejiang province and the Institutional Animal Care and Use Committee of Zhejiang University. Ten-week-old female (approximately 200 g) Sprague–Dawley rats were obtained from the Academy of Medical Sciences of Zhejiang province. Rats were anesthetized using isoflurane inhalation. The osteoporotic defect model in femur was constructed as previously reported [45–47]. Six weeks after OVX, a hole (3 mm in diameter and 3 mm in depth) was produced by a dental drill on the lateral side of left supracondylar femur [26,36]. The rats were randomly divided into the following three groups (n = 12 for each group): sham group, MAM group, MAM/SRT group, respectively. The amount of SRT2104 *in vivo* were estimated as mentioned in the previous study [10]. The total amount of SIRT2104 for each rat was approximately 100 μg. Then, the bone defect was filled with saline, MAM (3 mm in diameter and 3 mm in depth, 10 mg MAM) or MAM/SRT [3 mm in diameter and 3 mm in depth (10 mg MAM/SRT which included about 100 μg SRT2104)].

The rats were sacrificed via CO2 administration at 3 or 5 weeks after modeling. Next, the femur specimens were collected with 4% paraformaldehyde for 48 h.

6.21. Radiographic analysis and microcomputed tomography (micro-CT) evaluation

To evaluate callus formation and bridging bone formation at bone defect sites, Radiographs were taken using a dual-track molybdenum/rhodium + Mo target mammography machine (22 KV, 250 mAS; GE Healthcare, Fairfield, CT, USA). Immediately after, the samples were scanned using the μCT-100 imaging system (Scanco Medical, Brüttisellen, Switzerland) with X-ray energy settings of 70 kVp, 1024 reconstruction matrix, 14.8 μm slice thickness, and an exposure time of 300 ms. After reconstruction, a global threshold was used to segment the newly formed bone in accordance with previous studies [48,49]. After thresholding and segmentation, the bone volume fraction was calculated by three-dimensional standard microstructural analysis. Bone volume

Table 1
Sequences of primers for PCR analysis.

Gene	Reverse (5′-3′)	Reverse (3′-5′)
ALP	CCAACTCTTTTGTGCCAGAGA	GGCTACATTGGTGTTGAGCTTTT
Runx2	GACTGTGGTTACCGTCATGGC	ACTTGGTTTTTCATAACAGCGGA
COL1	CCACGTCTCACCATTGGGG	GCTCCTCTTAGGGGCCACT
GAPDH	CGACTTCAACAGCAACTCCCACTCTTCC	TGGGTGGTCCAGGGTTTCTTACTCCTT

Table 2
Antibodies information.

Antibody	Manufacture	Catalog number
OPN	Proteintech	22952-1-AP
Runx2	Cell Signaling Technology	#12556
SIRT1	Cell Signaling Technology	#8469
β-catenin	Cell Signaling Technology	#8480
GAPDH	Cell Signaling Technology	#5174
c-Fos	Abcam	ab222699
NFATc1	Abcam	ab25916
Ac-FoxO1	ImmunoWay Biotechnology	YK0110
Ac-FoxO3a	ImmunoWay Biotechnology	YK0112

Abbreviation: OPN, Osteopontin; Runx2, RUNX family transcription factor 2; SIRT1, Sirtuin 1; β-catenin, Catenin Beta 1; GAPDH, Glyceraldehyde-3-Phosphate Dehydrogenase; NFATc1, Nuclear Factor Of Activated T Cells 1; Ac-FoxO1, Acetylated Forkhead Box O1; Ac-FoxO3a, Acetylated Forkhead Box O3a.

(BV), total volume (TV), and bone volume fraction (BV/TV), trabecular number (Tb·N), trabecular thickness (Tb·Th), trabecular separation (Tb. Sp) were measured in the region of the bone defect as in previous studies [34,41,50].

6.22. Histological evaluation

Samples were decalcified using 10% EDTA (Sigma-Aldrich) with a solution change twice weekly for at least 8 weeks at 4 °C before embedding. Serial sections with a thickness of 5 μm were cut and mounted onto adhesion microscope slides (Ref. 188105, Citoglas, Beijing, China). Hematoxylin-eosin (HE) and TRAP staining were performed, as described in our previous study [43,50]. According to previous studies [51–53], the pathological parameters reflecting bone formation [BV/TV, Osteoblast number (N.Ob/B. Pm), the percent of Osteoid perimeter (%O. Pm)] and bone resorption [Osteoclast number (N.Oc/B. Pm)] were separately examined. Histomorphometric measurements were performed using OsteoMeasure software (OsteoMetrics, Decatur, GA). Three randomized high magnification (200 ×) fields of view were chosen. Immunohistochemical staining (IHC) of OPN was performed following manufacturers protocol. All antibodies information is listed in Table 2. IHC staining was semi-quantified in the bone healing part by ImageJ software [54].

6.23. Statistical analysis

Statistical analysis was performed using SPSS statistical software for Windows, version 18.0 (IBM, Armonk, NY, USA). All experiments were performed in at least triplicate, and the data are presented as the mean ± standard deviation. Statistical significance was determined between groups using a two-tailed Student's *t*-test or one-way analysis of variance (ANOVA) with Tukey's post hoc test. A value of $P \leq 0.05$ was considered statistically significant.

Funding

This study was supported by a grant from the National Natural Science Foundation of China (No. 81802221, 31870959, and 82102597), Zhejiang Provincial Natural Science Foundation of China (LY21H070001, LQ21H060007 and LY22H060006), and Zhejiang Undergraduate Talent Project (No. 2021R401214).

Data availability statement

All datasets presented in this study are included in the article.

Consent for publication

Not applicable.

Ethics approval and consent to participate

This study was carried out in accordance with the principles of the Basel Declaration and the recommendations of Zhejiang University. The protocol was approved by the Animal Ethics Committee of Zhejiang University (No.2021065).

CRediT authorship contribution statement

Wei Zhang: Conceptualization, Methodology, Investigation, Writing – original draft, Writing – review & editing. **Xingzhi Zhou:** Data curation, Writing – original draft. **Weiduo Hou:** Visualization, Data curation, Investigation, Project administration. **Erman Chen:** Visualization, Data curation, Investigation, Project administration. **Chenyi Ye:** Visualization, Data curation, Investigation, Project administration. **Mo Chen:** Visualization, Data curation, Investigation, Project administration. **Qian Lu:** Data curation, Writing – original draft. **Xiaohua Yu:** Conceptualization, Methodology, Investigation, Writing – original draft, Writing – review & editing. **Weixu Li:** Conceptualization, Methodology, Investigation, Writing – original draft, Writing – review & editing.

Declaration of competing interest

The authors declare that the research was conducted in the absence of any commercial or financial relationships that could be construed as a potential conflict of interest.

Abbreviations

BMSCs	Bone marrow-derived mesenchymal stem cells
siRNA	Small interfering RNA
CCK-8	Cell Counting Kit-8
IF	Immunofluorescence
RT-qPCR	Quantitative real-time polymerase chain reaction
WB	Western blot
micro-CT	Microcomputed tomography
OP	Osteoporosis
OVX	Ovariectomy
BMM	Bone marrow-derived macrophage
ALP	Alkaline phosphatase
OPN	Osteopontin
P1NP	Pro-collagen type 1N-terminal peptide;
FBS	Fetal bovine serum
SBF	Simulated body fluid
SEM	Scanning electron microscopy
XRD	X-ray diffraction
FTIR	Fourier transform infrared

Appendix A. Supplementary data

Supplementary data to this article can be found online at https://doi.org/10.1016/j.bioactmat.2022.04.017.

References

[1] D. The, Lancet, Endocrinology, Osteoporosis: overlooked in men for too long, Lancet Diabetes Endocrinol. 9 (1) (2021) 1.

[2] T. Lu, V. Forgetta, J. Keller-Baruch, M. Nethander, D. Bennett, M. Forest, S. Bhatnagar, R.G. Walters, K. Lin, Z. Chen, L. Li, M. Karlsson, D. Mellstrom, E. Orwoll, E.V. McCloskey, J.A. Kanis, W.D. Leslie, R.J. Clarke, C. Ohlsson, C.M. T. Greenwood, J.B. Richards, Improved prediction of fracture risk leveraging a genome-wide polygenic risk score, Genome Med. 13 (1) (2021) 16.

[3] F.B. Torstrick, R.E. Guldberg, Local strategies to prevent and treat osteoporosis, Curr. Osteoporos. Rep. 12 (1) (2014) 33–40.

[4] C.E. Jacome-Galarza, S.K. Lee, J.A. Lorenzo, H.L. Aguila, Parathyroid hormone regulates the distribution and osteoclastogenic potential of hematopoietic progenitors in the bone marrow, J. Bone Miner. Res. 26 (6) (2011) 1207–1216.

[5] G.J. Pettway, J.A. Meganck, A.J. Koh, E.T. Keller, S.A. Goldstein, L.K. McCauley, Parathyroid hormone mediates bone growth through the regulation of osteoblast proliferation and differentiation, Bone 42 (4) (2008) 806–818.

[6] H.N. Kim, L. Han, S. Iyer, R. de Cabo, H. Zhao, C.A. O'Brien, S.C. Manolagas, M. Almeida, Sirtuin 1 suppresses osteoclastogenesis by deacetylating FoxOs, Mol. Endocrinol. 29 (10) (2015) 1498–1509.

[7] K. Zainabadi, Drugs targeting SIRT1, a new generation of therapeutics for osteoporosis and other bone related disorders? Pharmacol. Res. 143 (2019) 97–105.

[8] R. Nogueiras, K.M. Habegger, N. Chaudhary, B. Finan, A.S. Banks, M.O. Dietrich, T. L. Horvath, D.A. Sinclair, P.T. Pfluger, M.H. Tschop, Sirtuin 1 and sirtuin 3: physiological modulators of metabolism, Physiol. Rev. 92 (3) (2012) 1479–1514.

[9] B.P. Hubbard, D.A. Sinclair, Small molecule SIRT1 activators for the treatment of aging and age-related diseases, Trends Pharmacol. Sci. 35 (3) (2014) 146–154.

[10] E.M. Mercken, S.J. Mitchell, A. Martin-Montalvo, R.K. Minor, M. Almeida, A. P. Gomes, M. Scheibye-Knudsen, H.H. Palacios, J.J. Licata, Y. Zhang, K.G. Becker, H. Khraiwesh, J.A. González-Reyes, J.M. Villalba, J.A. Baur, P. Elliott, C. Westphal, G.P. Vlasuk, J.L. Ellis, D.A. Sinclair, M. Bernier, R. de Cabo, SRT2104 extends survival of male mice on a standard diet and preserves bone and muscle mass, Aging Cell 13 (5) (2014) 787–796.

[11] I. Gurt, H. Artsi, E. Cohen-Kfir, G. Hamdani, G. Ben-Shalom, B. Feinstein, M. El-Haj, R. Dresner-Pollak, The Sirt1 activators SRT2183 and SRT3025 inhibit RANKL-induced osteoclastogenesis in bone marrow-derived macrophages and down-regulate Sirt3 in Sirt1 null cells, PLoS One 10 (7) (2015), e0134391.

[12] E. Hoffmann, J. Wald, S. Lavu, J. Roberts, C. Beaumont, J. Haddad, P. Elliott, C. Westphal, E. Jacobson, Pharmacokinetics and tolerability of SRT2104, a first-in-class small molecule activator of SIRT1, after single and repeated oral administration in man, Br. J. Clin. Pharmacol. 75 (1) (2013) 186–196.

[13] X. Yu, A.H. Biedrzycki, A.S. Khalil, D. Hess, J.M. Umhoefer, M.D. Markel, W. L. Murphy, Nanostructured mineral coatings stabilize proteins for therapeutic delivery, Adv. Mater. 29 (33) (2017).

[14] L. Jongpaiboonkit, T. Franklin-Ford, W.L. Murphy, Mineral-coated polymer microspheres for controlled protein binding and release, Adv. Mater. 21 (19) (2009) 1960–1963.

[15] W. Li, K. Sheng, Y. Ran, J. Zhang, B. Li, Y. Zhu, J. Chen, Q. He, X. Chen, J. Wang, T. Jiang, X. Yu, Z. Ye, in: Transformation of Acellular Dermis Matrix with Dicalcium Phosphate into 3D Porous Scaffold for Bone Regeneration, J Biomater Sci Polym, 2021, pp. 1–17.

[16] L. Jongpaiboonkit, T. Franklin-Ford, W.L. Murphy, Growth of hydroxyapatite coatings on biodegradable polymer microspheres, ACS Appl. Mater. Interfaces 1 (7) (2009) 1504–1511.

[17] L. Zhang, L. Liu, R. Thompson, C. Chan, CREB modulates calcium signaling in cAMP-induced bone marrow stromal cells (BMSCs), Cell Calcium 56 (4) (2014) 257–268.

[18] P. Ducy, R. Zhang, V. Geoffroy, A.L. Ridall, G. Karsenty, Osf2/Cbfa1: a transcriptional activator of osteoblast differentiation, Cell 89 (5) (1997) 747–754.

[19] C. Ye, M. Chen, E. Chen, W. Li, S. Wang, Q. Ding, C. Wang, C. Zhou, L. Tang, W. Hou, K. Hang, R. He, Z. Pan, W. Zhang, Knockdown of FOXA2 enhances the osteogenic differentiation of bone marrow-derived mesenchymal stem cells partly via activation of the ERK signalling pathway, Cell Death Dis. 9 (8) (2018) 836.

[20] A.I. Garbe, A. Roscher, C. Schuler, A.H. Lutter, M. Glosmann, R. Bernhardt, M. Chopin, U. Hempel, L.C. Hofbauer, S. Rammelt, M. Egerbacher, R.G. Erben, R. Jessberger, Regulation of bone mass and osteoclast function depend on the F-actin modulator SWAP-70, J. Bone Miner. Res. 27 (10) (2012) 2085–2096.

[21] J.M. Baek, J.Y. Kim, S.J. Ahn, Y.H. Cheon, M. Yang, J. Oh, M.K. Choi, Dendrobium moniliforme exerts inhibitory effects on both receptor activator of nuclear factor kappa-B ligand-mediated osteoclast differentiation in vitro and lipopolysaccharide-induced bone erosion in vivo, Molecules 21 (3) (2016) 295.

[22] K. Henriksen, J. Bollerslev, V. Everts, M.A. Karsdal, Osteoclast activity and subtypes as a function of physiology and pathology–implications for future treatments of osteoporosis, Endocr. Rev. 32 (1) (2011) 31–63.

[23] W. Seo, S. Lee, P.T. Tran, T.Q. Ngo, O. Kim, T.H. Le, N.H. Dang, C. Hwangbo, B. S. Min, J.H. Lee, 3-Hydroxyolean-12-en-27-oic acids inhibit RANKL-induced osteoclastogenesis in vitro and inflammation-induced bone loss in vivo, Int. J. Mol. Sci. 21 (15) (2020).

[24] J.H. Kim, B.U. Youn, K. Kim, J.B. Moon, J. Lee, K.I. Nam, Y.W. Park, D.D. O'Leary, K.K. Kim, N. Kim, Lhx2 regulates bone remodeling in mice by modulating RANKL signaling in osteoclasts, Cell Death Differ. 21 (10) (2014) 1613–1621.

[25] J. Lorenzo, The many ways of osteoclast activation, J. Clin. Invest. 127 (7) (2017) 2530–2532.

[26] D.A. Callaway, J.X. Jiang, Reactive oxygen species and oxidative stress in osteoclastogenesis, skeletal aging and bone diseases, J. Bone Miner. Metabol. 33 (4) (2015) 359–370.

[27] J. Zhang, F. He, W. Zhang, M. Zhang, H. Yang, Z.P. Luo, Mechanical force enhanced bony formation in defect implanted with calcium sulphate cement, Bone Res 3 (2015) 14048.

[28] R. Dong, Y. Bai, J. Dai, M. Deng, C. Zhao, Z. Tian, F. Zeng, W. Liang, L. Liu, S. Dong, Engineered scaffolds based on mesenchymal stem cells/preosteoclasts extracellular matrix promote bone regeneration, J. Tissue Eng. 11 (2020), 204173142092691.

[29] S. Ray, U. Thormann, M. Eichelroth, M. Budak, C. Biehl, M. Rupp, U. Sommer, T. El Khassawna, F.I. Alagboso, M. Kampschulte, M. Rohnke, A. Henss, K. Peppler, V. Linke, P. Quadbeck, A. Voigt, F. Stenger, D. Karl, R. Schnettler, C. Heiss, K. S. Lips, V. Alt, Strontium and bisphosphonate coated iron foam scaffolds for osteoporotic fracture defect healing, Biomaterials 157 (2018) 1–16.

[30] M.L. Bouxsein, S.K. Boyd, B.A. Christiansen, R.E. Guldberg, K.J. Jepsen, R. Müller, Guidelines for assessment of bone microstructure in rodents using micro-computed tomography, J. Bone Miner. Res. 25 (7) (2010) 1468–1486.

[31] C. Chen, M. Zhou, Y. Ge, X. Wang, SIRT1 and aging related signaling pathways, Mech. Ageing Dev. 187 (2020) 111215.

[32] W. Sun, W. Qiao, B. Zhou, Z. Hu, Q. Yan, J. Wu, R. Wang, Q. Zhang, D. Miao, Overexpression of Sirt1 in mesenchymal stem cells protects against bone loss in mice by FOXO3a deacetylation and oxidative stress inhibition, Metabolism 88 (2018) 61–71.

[33] L. Ling, C. Dombrowski, K.M. Foong, L.M. Haupt, G.S. Stein, V. Nurcombe, A.J. van Wijnen, S.M. Cool, Synergism between Wnt3a and heparin enhances osteogenesis via a phosphoinositide 3-kinase/Akt/RUNX2 pathway, J. Biol. Chem. 285 (34) (2010) 26233–26244.

[34] W. Zhang, E. Chen, M. Chen, C. Ye, Y. Qi, Q. Ding, H. Li, D. Xue, X. Gao, Z. Pan, IGFBP7 regulates the osteogenic differentiation of bone marrow-derived mesenchymal stem cells via Wnt/beta-catenin signaling pathway, Faseb. J. 32 (4) (2018) 2280–2291.

[35] Y. Chen, F. Zhou, H. Liu, J. Li, H. Che, J. Shen, E. Luo, SIRT1, a promising regulator of bone homeostasis, Life Sci. 269 (2021) 119041.

[36] Z. Liu, L. Dong, L. Wang, X. Wang, K. Cheng, Z. Luo, W. Weng, Mediation of cellular osteogenic differentiation through daily stimulation time based on polypyrrole planar electrodes, Sci. Rep. 7 (1) (2017) 17926.

[37] J. Chen, X. Zhou, W. Sun, Z. Zhang, W. Teng, F. Wang, H. Sun, W. Zhang, J. Wang, X. Yu, Z. Ye, W. Li, Vascular derived ECM improves therapeutic index of BMP-2 and drives vascularized bone regeneration, Small (2022), e2107991.

[38] B.B. Koh, E.J. Lee, K. Ramachandraiah, G.P. Hong, Characterization of bovine serum albumin hydrolysates prepared by subcritical water processing, Food Chem. 278 (2019) 203–207.

[39] H. Zhu, Z.-K. Guo, X.-X. Jiang, H. Li, X.-Y. Wang, H.-Y. Yao, Y. Zhang, N. Mao, A protocol for isolation and culture of mesenchymal stem cells from mouse compact bone, Nat. Protoc. 5 (3) (2010) 550–560.

[40] W. Zhang, W. Hou, M. Chen, E. Chen, D. Xue, C. Ye, W. Li, Z. Pan, Upregulation of parkin accelerates osteoblastic differentiation of bone marrow-derived mesenchymal stem cells and bone regeneration by enhancing autophagy and beta-catenin signaling, Front. Cell Dev. Biol. 8 (2020) 576104.

[41] E.E.M. Chen, W. Zhang, C.C.Y. Ye, X. Gao, L.L.J. Jiang, T.T.F. Zhao, Z.Z.J. Pan, D.D. T. Xue, Knockdown of SIRT7 enhances the osteogenic differentiation of human bone marrow mesenchymal stem cells partly via activation of the Wnt/beta-catenin signaling pathway, Cell Death Dis. 8 (9) (2017), e3042.

[42] C. Ye, W. Zhang, K. Hang, M. Chen, W. Hou, J. Chen, X. Chen, E. Chen, L. Tang, J. Lu, Q. Ding, G. Jiang, B. Hong, R. He, Extracellular IL-37 promotes osteogenic differentiation of human bone marrow mesenchymal stem cells via activation of the PI3K/AKT signaling pathway, Cell Death Dis. 10 (10) (2019) 753.

[43] C. Ye, W. Hou, M. Chen, J. Lu, E. Chen, L. Tang, K. Hang, Q. Ding, Y. Li, W. Zhang, R. He, IGFBP7 acts as a negative regulator of RANKL-induced osteoclastogenesis and oestrogen deficiency-induced bone loss, Cell Prolif 53 (2) (2020), e12752.

[44] S. Pal, S.K. Maurya, S. Chattopadhyay, S. Pal China, K. Porwal, C. Kulkarni, S. Sanyal, R.A. Sinha, N. Chattopadhyay, The osteogenic effect of liraglutide involves enhanced mitochondrial biogenesis in osteoblasts, Biochem. Pharmacol. 164 (2019) 34–44.

[45] Z. Xie, S. Weng, H. Li, X. Yu, S. Lu, K. Huang, Z. Wu, B. Bai, V. Boodhun, L. Yang, Teriparatide promotes healing of critical size femur defect through accelerating angiogenesis and degradation of beta-TCP in OVX osteoporotic rat model, Biomed. Pharmacother. 96 (2017) 960–967.

[46] Y. Zhang, N. Cheng, R. Miron, B. Shi, X. Cheng, Delivery of PDGF-B and BMP-7 by mesoporous bioglass/silk fibrin scaffolds for the repair of osteoporotic defects, Biomaterials 33 (28) (2012) 6698–6708.

[47] K.C. Li, Y.H. Chang, C.L. Yeh, Y.C. Hu, Healing of osteoporotic bone defects by baculovirus-engineered bone marrow-derived MSCs expressing MicroRNA sponges, Biomaterials 74 (2016) 155–166.

[48] Z. Zhang, Y. Wang, W. Teng, X. Zhou, Y. Ye, H. Zhou, H. Sun, F. Wang, A. Liu, P. Lin, W. Cui, X. Yu, Y. Wu, Z. Ye, An orthobiologics-free strategy for synergistic photocatalytic antibacterial and osseointegration, Biomaterials 274 (2021) 120853.

[49] B. Yuan, L. Wang, R. Zhao, X. Yang, X. Yang, X. Zhu, L. Liu, K. Zhang, Y. Song, X. Zhang, A biomimetically hierarchical polyetherketoneketone scaffold for osteoporotic bone repair, Sci. Adv. 6 (50) (2020).

[50] W. Zhang, D. Xue, H. Yin, S. Wang, C. Li, E. Chen, D. Hu, Y. Tao, J. Yu, Q. Zheng, X. Gao, Z. Pan, Overexpression of HSPA1A enhances the osteogenic differentiation of bone marrow mesenchymal stem cells via activation of the Wnt/beta-catenin signaling pathway, Sci. Rep. 6 (2016) 27622.
[51] Y. Wang, P. Deng, Y. Liu, Y. Wu, Y. Chen, Y. Guo, S. Zhang, X. Zheng, L. Zhou, W. Liu, Q. Li, W. Lin, X. Qi, G. Ou, C. Wang, Q. Yuan, Alpha-ketoglutarate ameliorates age-related osteoporosis via regulating histone methylations, Nat. Commun. 11 (1) (2020) 5596.
[52] L. Zheng, Z. Zhuang, Y. Li, T. Shi, K. Fu, W. Yan, L. Zhang, P. Wang, L. Li, Q. Jiang, Bone targeting antioxidative nano-iron oxide for treating postmenopausal osteoporosis, Bioact. Mater. 14 (2022) 250–261.
[53] D.W. Dempster, J.E. Compston, M.K. Drezner, F.H. Glorieux, J.A. Kanis, H. Malluche, P.J. Meunier, S.M. Ott, R.R. Recker, A.M. Parfitt, Standardized nomenclature, symbols, and units for bone histomorphometry: a 2012 update of the report of the ASBMR Histomorphometry Nomenclature Committee, J. Bone Miner. Res. 28 (1) (2013) 2–17.
[54] K. Hu, B.R. Olsen, Osteoblast-derived VEGF regulates osteoblast differentiation and bone formation during bone repair, J. Clin. Invest. 126 (2) (2016) 509–526.